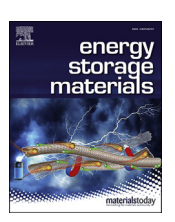
ELSEVIER

Contents lists available at ScienceDirect

Energy Storage Materials

journal homepage: www.elsevier.com/locate/ensm



Synergistic H⁺/Zn²⁺ dual ion insertion mechanism in high-capacity and ultra-stable hydrated VO₂ cathode for aqueous Zn-ion batteries



Kaiyue Zhu^{a,1}, Tao Wu^{a,1}, Shichen Sun^a, Wessel van den Bergh^b, Morgan Stefik^b, Kevin Huang^{a,*}

- ^a Department of Mechanical Engineering, University of South Carolina, Columbia, SC, 29201, USA
- ^b Department of Chemistry and Biochemistry, University of South Carolina, Columbia, SC, 29201, USA

ARTICLE INFO

Keywords:
Zinc-ion battery
Hydrated VO₂ cathode
H⁺/Zn²⁺co-insertion
Mechanism
Zn(OH)₂ nanoflakes

ABSTRACT

Rechargeable aqueous zinc ion batteries (ZIB) with near-neutral electrolytes are a promising candidate for stationary energy storage owing to their high-energy-density, high-safety, low-cost and environmental-friendliness. However, the development of ZIBs is currently hindered by the lack of high-performance cathode materials and a good understanding of the true ionic storage mechanism in cathodes. Herein, using a promising ZIB cathode, hydrated VO₂ (denoted as H-VO₂), as a model material, we carried out a systematic experimental and theoretical work to elucidate the ionic storage mechanisms. We show strong evidence that H^+ and Zn^{2+} are synergistically involved in the ionic storage in H-VO₂. The H^+ -insertion/extraction, which leads to a pH swing of the electrolyte, can be viewed as an indirect Zn^{2+} -storage through a reversible precipitation/dissolution of $Zn(OH)_2$ on the surface of H-VO₂ cathode. The first-principles DFT calculations further reveal that H^+ and Zn^{2+} have their own favorable insertion sites and migration pathways, but H^+ -insertion predominates in the initial discharge stage whereas Zn^{2+} -insertion controls in the late discharge stage. Because of the synergetic H^+/Zn^{2+} co-insertion, H^- VO₂-based ZIB exhibits a high capacity and stability at both low and high rates, e.g. 410 and 200 mAh g^{-1} , 88% and 70% retention rate for 200 (~1500 h) and 3000 cycles (~215 h) at 0.1 and 5.0 A g^{-1} , respectively. The new fundamental insights gained from this study deepen the understanding of aqueous Zn-ion battery chemistry for future development of advanced ZIB cathodes.

1. Introduction

The increasing demand for clean energy to mitigate global warming and climate change has sparked a swift commercial development of renewable energies (such as solar, wind, tidal, etc.) in recent decades [1]. However, the intermittent power production from renewable sources requires a viable "buffering" solution to make it energy efficient and cost effective for market entry. Recently, rechargeable aqueous Zn-ion batteries (ZIBs) with neutral electrolytes emerge as a promising solution for large-scale renewable energy storage (LSRES) [2–6]. Like the conventional alkaline Zn-batteries, e.g. Zn–MnO₂, Zn–Ni and Zn-air, ZIBs also use low-cost, low-potential and high-energy-density Zn metal as the anode. However, the major difference is that ZIBs employ a neutral Zn²⁺-conducting electrolyte, whereas the alkaline Zn-batteries use KOH as the electrolyte. The advantage of using neutral electrolytes vs alkaline electrolytes is that the former avoids the irreversible formation of

 $Zn(OH)_2/ZnO$ phases and mitigates Zn-dendrite growth, thus ensuring high capacity and reversibility [7–12].

It is generally understood that the Zn²⁺-storing cathode is a performance limiting component in ZIBs, and thus a major hurdle to the successful product development of ZIBs [2,3,13–15]. The challenge to improve Zn²⁺-storage performance is rooted in the sluggish kinetics of Zn²⁺-insertion/extraction, resulted from the higher charge/radius ratio of Zn²⁺ and stronger electrostatic interactions between Zn²⁺ and other ions in the cathode materials [2]. So far, materials with tunnel or layered structures have been studied as the cathodes of ZIBs, examples of which include Prussian blue analogs, manganese-based oxides, and V-based oxides [10,16–25]. Early studies have shown Prussian blue analogs with a tunnel structure and Mn-based oxides with a tunnel or layered structure can store Zn²⁺, but suffer from either low capacity or poor cycling stability in Zn²⁺-based mild electrolyte [26–30]. Recent development, however, has indicated that capacity and cycle stability of Zn/MnO₂

E-mail address: huang46@cec.sc.edu (K. Huang).

^{*} Corresponding author.

¹ These authors contributed equally to this work.

batteries can be significantly improved by adding MnSO₄ into the electrolyte as a result of mitigated Mn-dissolution [30-36]. In comparison, recent studies show V-based oxides (such as V2O5·nH2O, VO2, H2V3O8, $Na_2V_6O_{16} \cdot nH_2O$, $NaCa_{0.6}V_6O_{16} \cdot nH_2O$, $Zn_{0.25}V_2O_5 \cdot nH_2O$, $Ca_{0.25}V_2O_5 \cdot nH_2O$ O₅·nH₂O, Zn₃V₂O₇(OH)₂·nH₂O) are better ZIB cathodes with higher energy density and longer cycle life [37-45]. Among these materials, VO₂ with a tunnel framework structure is an interesting cathode because of its high-rate capability and controversial mechanisms for Zn²⁺-storage. According to the studies by Mai et al., Myung et al., and Yang et al., Zn²⁺ is the only mobile ion that moves in and out of the VO2 structure during discharge and charge [38,46,47]. In contrast, Wagemaker et al. argue that only H⁺ can be inserted into VO₂ cathode accompanied by a Zn²⁺ storage mechanism through the reversible deposition Zn₄SO₄(OH)₆·5H₂O (with a ZnSO₄ electrolyte) on the cathode surface [48]. So far, there is still no consensus on the actual mechanism of Zn²⁺-storage in VO₂. Due to the possible H⁺ involvement, Zn²⁺-insertion based storage mechanisms for other ZIB cathodes are also being questioned. Therefore, it is necessary to further explore the storage mechanisms of ZIB cathodes and gain mechanistic insights for the design and optimization of future advanced ZIB cathode materials.

Assisted by a combined experimental and theoretical approach, herein we report a systematic study on the ionic storage mechanisms in ZIB employing hydrated VO₂ (H-VO₂) as a model cathode. We show direct evidence of synergistic dual ${\rm Zn}^{2+}/{\rm H}^+$ insertion in H-VO₂ structure through carefully designed electrochemical experiments, structural/compositional analyses as well as DFT calculations, and conclude that both H⁺ and ${\rm Zn}^{2+}$ can be reversibly inserted/extracted into/from H-VO₂ structure in a synergistic manner. Such dual-ion insertion mechanisms enable a H-VO₂-based ZIB to achieve high capacity and stability at both low and high rates. Beyond the demonstration of H-VO₂ as a promising high-capacity and high-durability cathode candidate, the mechanistic insights gained from this study deepen out understanding of the ionic storage mechanisms in aqueous ZIBs in general and lay the foundation for future discovery of new advanced cathodes.

2. Experimental section

2.1. Synthesis of hydrated VO2 nanobelts

The hydrated VO $_2\cdot0.45H_2O$ (denoted as H-VO $_2$) nanorods were prepared through a facile and scalable hydrothermal method [49]. In a typical procedure, 0.6 g V $_2O_5$ and 1.2 g H $_2C_2O_4\cdot2H_2O$ were first dissolved in 20 mL deionized (DI) water under vigorous stirring at 90 °C for 5 h to form a blue solution. Then 4 mL of H $_2O_2$ (35 wt%) was added to the blue solution, followed by stirring the mixture for 30 min. A 50 mL ethanol was then added into the mixture and stirred for another 1 h. The formed dark-green mixture was subsequently loaded into a 100 mL autoclave with a Teflon liner and held at 170 °C for 12 h. Finally, the precipitate was collected and thoroughly washed with deionized water and ethanol, and dried at 60 °C for 12 h.

2.2. Materials characterization

Phase and structure determination. X-ray diffraction (XRD) patterns of the H-VO₂ samples were collected using a Rigaku D/MAX-2100 with Cu Kα radiation ($\lambda=1.5418$ Å). The data were recorded from 5° to 120° with an interval of 0.02° and a scan speed of 2° min⁻¹. The Rietveld refinements were performed on the collected XRD patterns using TOPAS. *In situ* transmissive XRD was conducted using SAXSLab Ganesha. A Xenocs GeniX 3D microfocus source was used with a copper target to produce a monochromatic beam with a 0.154 nm wavelength. The wide-angle X-ray scattering (WAXS) data were acquired with an X-ray flux of ~36.3 M photon per second incident upon the sample and a sample-to-detector distance of 90 mm under atmospheric conditions (vented) due to the use of aqueous electrolyte. A BioLogic SP-150 was used for electrochemical measurements during *in situ* battery cycling at a current density

of 0.2 A g⁻¹, while WAXS data were acquired continuously during *in situ* cycling with a 10-min exposure per frame.

Microstructure. The morphologies of the samples were captured with a Zeiss Ultra plus field emission scanning electron microscope (FESEM). The crystalline structures and morphologies of samples were also acquired with a high-resolution transmission electron microscope (HRTEM, H9500) operated at 300 kV. Elemental mapping along with morphology were obtained by a scanning transmission electron microscope (STEM, HD2000) equipped with an energy-dispersive X-ray spectrometer (EDS).

Surface chemistry. The surface chemical compositions and oxidation states of the elements were analyzed by X-ray photoelectron spectroscopy (XPS, Kratos AXIS Ultra DLD) with Al Ka X-ray radiation (h $\nu=1486.6\text{eV}$). Prior to these analysis, the cycled electrode powders were washed thoroughly with DI water to remove electrolyte residue and then dried in a glove box. All the binding energies were corrected by adventitious C 1s at 284.6 eV.

Thermal analysis. Thermogravimetric analysis (TGA) was performed using a Netzsch STA 448 TGA/DSC thermal analyzer to determine the water content in the samples. Specimens were placed in a $\rm Al_2O_3$ crucible with a lid, and TGA data were recorded under a flow $\rm N_2$ at 50 mL min $^{-1}$, while ramping from room temperature to 600 °C at a rate of 2 °C min $^{-1}$, and then cooling naturally to room temperature. Before the TG measurement, H-VO $_2$ powders were dried in a vacuum oven at 100 °C for at least 2 h.

Specific surface area analysis. Brunauer-Emmett-Teller (BET) specific surface areas of samples were analyzed by a Quantachrome QUAD-RASORB SI instrument using their physical adsorption at 77.3 K.

Solid-state ¹H nuclear magnetic resonance (NMR) analysis. The solidstate ¹H NMR spectra of relevant samples were collected on a 500 MHz superconducting NMR spectrometer (Bruker AMX500).

2.3. Electrochemical characterization

Battery cell assembly. Electrochemical tests were carried out using CR2032-type coin cells. To prepare a H-VO₂ electrode, 60 wt% H-VO₂ nanorods, 26 wt% Super-P, and 14 wt% polyvinylidene fluoride (PVDF) were thoroughly mixed and dispersed into N-Methyl pyrrolidone (NMP). The resultant slurry was then coated uniformly onto a 14 mm diameter stainless steel mesh, resulting in a $\sim\!2$ mg cm $^{-2}$ active mass loading, followed by vacuum drying at 100 °C for $\sim\!12$ h and compression at 10 MPa. In a full ZIB cell, zinc foil was used as the anode, 3 M Zn(CF₃SO₃)₂ as the electrolyte, and glass microfiber filters (Whatman, Grade GF/A) as the separator.

Electrochemical testing. The CR2032-type coin cells were assembled in air and tested using a LAND battery testing system (CT2001A) within a potential window of $0.35-1.35~V~(vs~Zn/Zn^{2+})$. Cyclic voltammograms (CV) and electrochemical impedance spectroscopy (EIS) were performed in a three-electrode configuration using a solartron 1260/1287 electrochemical workstation. A Zn-ring and carbon paper were used as reference and counter electrode, respectively. The EIS measurement were carried out under open circuit voltage (OCV) with an AC amplitude of 10~mV in a frequency range of 100~KHz and 0.1~Hz in a temperature-controlled oven. The galvanostatic intermittent titration technique (GITT) was employed to determine Zn^{2+} diffusivity using a series of galvanostatic discharge pulses of 10~mi at $60~mA~g^{-1}$, followed by a 1~h relaxation. The Zn^{2+} diffusion coefficient ($D_{Zn^{2+}}$ GiTT) is calculated by Ref. [50]:

$$D_{Zn^{2+}}^{GITT} = \frac{4L^2}{\pi\tau} \left(\frac{\Delta E_s}{\Delta E_t}\right)^2 \tag{1}$$

where τ is the constant current pulse time; L corresponds to the Zn^{2+} diffusion length, which equals the thickness of the electrode; ΔE_s is the change of steady-state voltage during a single-step GITT experiment, and ΔE_t is the change in cell voltage at a constant current minus IR-loss during each galvanic step.

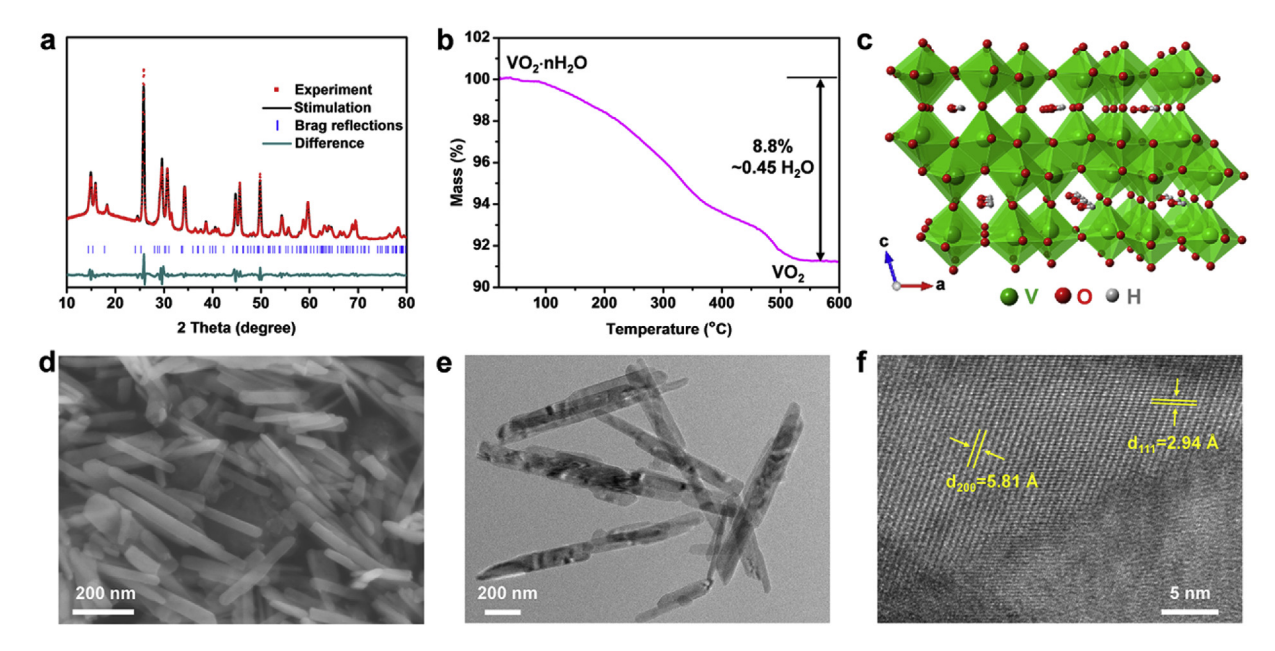


Fig. 1. Structural and morphology characterization of H-VO_2 . (a) Experimental (red dot) and Rietveld-refined (black line) XRD patterns of as-prepared H-VO_2 . Tick marks in blue and bottom curve in dark cyan indicate the allowed Bragg reflections and difference between experiment and refinement, respectively. (b) TGA curves under a dry N_2 atmosphere. (c) View of H-VO_2 structure along the b-axis. (d) SEM, (e) TEM and (f) HRTEM images of H-VO_2 . (For interpretation of the references to colour in this figure legend, the reader is referred to the Web version of this article.)

2.4. First-principle DFT calculations

All DFT calculations were performed by Perdew-Burke-Ernzerhof (PBE) generalized gradient approximation (GGA) exchange-correlation method, as implemented in the Vienna ab Initio Simulation Package (VASP) [51-54]. The projector augmented wave (PAW) method was used to calculate the interaction between core electrons and valence electrons. Valence configurations include the H (1s¹), O (2s²2p⁴), V (3p⁶3d⁴4s¹) and Zn (3d104p2) states [55]. All calculations were run with a cutoff energy of 400 eV, Gaussian smearing and normal precision. For thermodynamic calculations such as lattice parameters and voltage, we employed the DFT + U formalism developed by Anisimov et al. to account for strong on-site Coulombic interactions of the V 3d-electrons, with a specific on-site potential of U = 4.0 eV [56]. To explicitly account for van der Waals' interactions between layers and structural water, van der Waals-corrected D3 method developed by Grimme was used [57]. To consider the magnetism of VO2, the spin polarized calculations were performed to determine the ground state. Herein, the ferromagnetic VO2 was determined as the ground state and was used for all thermodynamic calculations. The lattice constants and atomic positions were both fully relaxed until a maximum energy difference and residual force on atoms converge were reached at 10⁻⁴ eV and 0.01 eV/Å, respectively. The Brillouin zone was sampled with 3 \times 6 \times 3 K-point to predict the lattice constants for the unit cell of VO₂·0.5H₂O.

To model ionic diffusion in the host structure, we employed climbing-image nudged elastic band (CI-NEB) method to couple with density functional theory (DFT) [58,59]. We selected to use DFT instead of DFT + U because an early first-principles calculation of multivalent-ion migration in oxide spinels has shown a pronounced metastability of electronic states along the ion migration path with U, resulting in a poor computational convergence. The study also reported that no significant improvements in the diffusion barriers were found using DFT + U calculations. The convergence threshold of the total energy was set to $1\times10^{-4}~\rm eV$, and a tolerance of 0.02 eV/A for the forces was used in the CI-NEB procedure. A total of eight images were interpolated between the initial and final relaxed structures in each case.

Based on the total energies of $VO_2 \cdot 0.5H_2O$ and various ion-insertion configurations, the voltage profile for a VO_2 electrode at 0 K with H^+

and Zn^{2+} co-insertion can be determined by:

$$V_{1} = -\frac{E(H_{x_{2}}VO_{2} \cdot 0.5H_{2}O) - E(H_{x_{1}}VO_{2} \cdot 0.5H_{2}O) - E(H)}{(x_{2} - x_{1})e}, \ x_{2} > x_{1}$$
 (2)

$$V_{2} = -\frac{E(Zn_{y_{2}}VO_{2} \cdot 0.5H_{2}O) - E(Zn_{y_{1}}VO_{2} \cdot 0.5H_{2}O) - E(Zn)}{(y_{2} - y_{1})e}, y_{2} > y_{1}$$
 (3)

where V_1 and V_2 are the average voltages for H^+ and Zn^{2+} insertion, respectively; E(H) is the energy of a single H atom, which is calculated from the relaxed H_2 structure; and E(Zn) is the Gibbs free energy per atom calculated from bulk Zn (hcp). Other Es represent the total energy of the specified material. x_1 and x_2 represent H^+ concentrations at two different SOCs, while y_1 and y_2 represent Zn^{2+} concentrations at two different SOCs. It should be noted that the simulated potential of H^+ insertion is versus standard hydrogen electrode (SHE), which should be converted to the Zn/Zn^{2+} potential for comparison with the experiment data [48]; the latter is referenced versus Zn metal. The overall dual Zn^{2+}/H^+ insertion reaction can be written by:

$$\frac{1}{2}\text{Zn} + H_2\text{O} + \text{V}O_2 \cdot 0.5H_2\text{O} \rightarrow \frac{1}{2}\text{Zn}(OH)_2 + H\text{V}O_2 \cdot 0.5H_2\text{O}$$
 (4)

The anodic reaction is:

$$Zn \rightarrow Zn^{2+} + 2e^{-} \tag{5}$$

The cathodic reaction follows:

$$H^{+} + e^{-} + VO_{2} \cdot 0.5H_{2}O \rightarrow HVO_{2} \cdot 0.5H_{2}O$$
 (6)

in conjunction with reactions in the electrolyte solution $% \left(1\right) =\left(1\right) \left(1\right) \left($

$$H_2O = H^+ + OH^- (7)$$

$$Zn^{2+} + 2(OH)^{-} \to Zn(OH)_{2}$$
 (8)

Based on the reduction potential for the following reaction at pH = 0:

$$Zn(OH)_2 + 2e^- \rightarrow Zn + 2(OH)^-, E^0 = -0.416 V \text{ (pH} = 0)$$
 (9)

The voltage difference between hydrogen and Zn metal will be equal

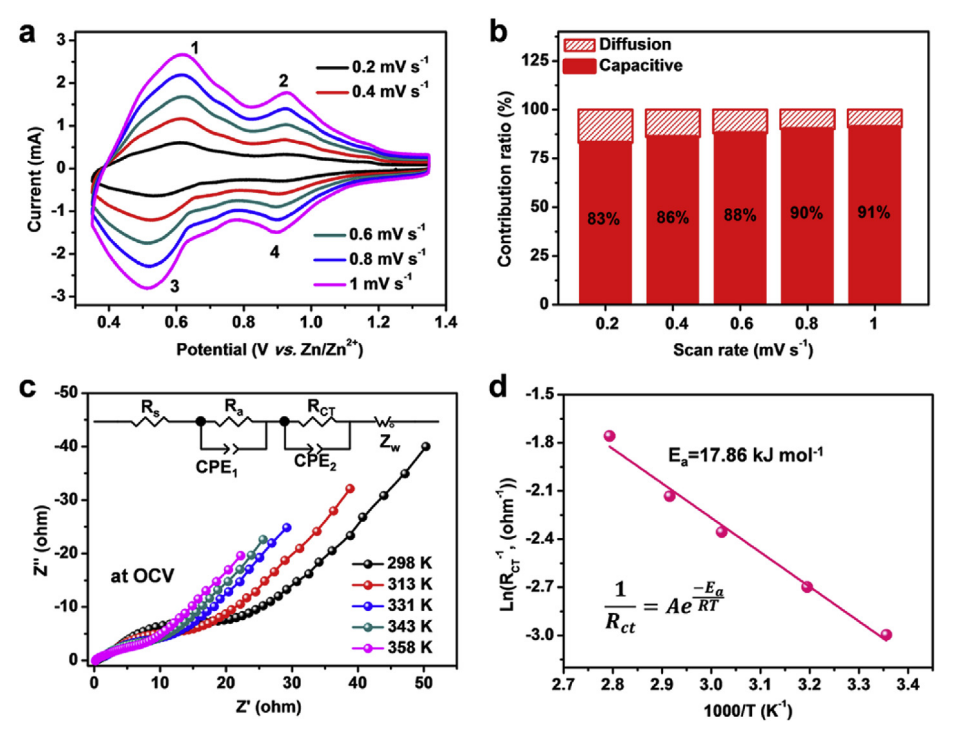


Fig. 2. Electrochemical behavior of H-VO $_2$ electrode in 3 M Zn(CF $_3$ SO $_3$) $_2$ electrolyte using three-electrode cell (RE: Zn ring, CE: carbon paper). (a) CV curves at various scan rates. (b) Capacity contribution ratios at various scan rates. (c) EIS spectra at OCV state of H-VO $_2$ cathode measured at various temperatures. Inset: equivalent circuit used in the fitting. R $_5$, ohmic resistance; R $_4$, surface absorption resistance; R $_{CT}$, charge transfer resistance; CPE, constant phase element; Z $_w$, Warburg impedance; (d) Plots of ln (R $_{CT}$ 1) versus 1000/T.

to the reduction potential (pH = 0) of eq. (9):

$$\Delta E = -0.416 \text{ V} \tag{10}$$

Finally, the average voltage curve for H insertion into $VO_2 \cdot 0.5H_2O$ versus SHE could be corrected and given versus Zn/Zn^{2+} by:

$$V' = V_1 - \frac{\Delta E}{2} = V_1 + 0.208 V \tag{11}$$

In addition, the actual H^+ concentration could also alter the H^+ insertion voltage, namely, $V=V^{\cdot}-\frac{\Delta G_{pH}}{e}.$ Herein, ΔG_{pH} is the Gibbs free energy of H^+ corrected by concentration. It equals $\Delta G_{pH}=2.303\times k_BT\times pH,$ where k_B is the Boltzmann constant and the pH value is set to 5 in this work to be consistent with the experimental value.

3. Results and discussion

3.1. Characterization of the synthesized hydrated VO₂ (H-VO₂)

The phase purity and morphology of the as-prepared VO2 were examined by XRD, Raman spectroscopy, scanning electron microscopy (SEM) and transmission electron microscopy (TEM), respectively. Shown in Fig. 1a is the XRD pattern along with Rietveld refinement, indicating that H-VO₂ has a monoclinic structure (space group of C2/m) with lattice parameters of a = 12.0589(9) Å, b = 3.6976(0) Å, c = 6.4225(5) Å, $\alpha = \gamma$ = 90°, β = 107.0°. The reliability factors of the refinement are excellent, achieving GOF = 3.43, $R_p = 4.42\%$ and $R_{wp} = 6.75\%$. Thermogravimetric analyses (TGA) of Fig. 1b suggest that the number of tunnel water per VO₂ is 0.45. Based on XRD patterns of Fig. 1a, the crystal structure of VO₂·0.5H₂O created by CrystalMaker (for building a simple crystal unit cell, 0.5H₂O per VO₂ was adopted instead for illustration purpose) is shown in Fig. 1c, in which distorted VO₆ octahedra are either corner shared or edge shared to form a tunnel framework, and some tunnels are occupied by the structural water (tunnel water). The identification of VO₂·0.45H₂O (denoted as H-VO₂) is also supported by Raman spectrum shown in Fig. S1, where detailed vibration mode assignments are given. The SEM and TEM images of Fig. 1d and e reveal H-VO2 crystalized in a nanorod morphology with a width of ~70 nm and length of ~300 nm.

The high resolution (HR) TEM shown in Fig. 1f clearly indicates two different lattice fringes. The lattice spacings are 5.81 and 2.94 Å, which are in line with the (200) and (111) lattice planes of H-VO₂, respectively. The BET surface area analysis shown in Fig. S2 indicates that the asprepared H-VO₂ has a specific surface area of $106 \text{ m}^2 \text{ g}^{-1}$.

3.2. Electrochemical behavior of single H-VO2 electrode

Before assembling a full battery cell, the electrochemical performance of H-VO $_2$ in aqueous 3 M Zn(CF $_3$ SO $_3$) $_2$ electrolyte was first investigated by cyclic voltammetry (CV) and electrochemical impedance spectroscopy (EIS) using a three-electrode cell configuration (Counter electrode (CE): carbon paper; Reference electrode (RE): Zn ring); the three-electrode setup is shown in Fig. S3a. Fig. 2a shows the CV curves of H-VO $_2$ measured at various scan rates from 0.2 to 1.0 mV s $^{-1}$, revealing that all curves have a similar shape with two major pairs of redox peaks at 0.61/0.53V and 0.92/0.91V, respectively.

From the CV profiles, the peak current (i) and scan rate (ν) are correlated by power law $i = av^b$, from which the b-values are obtained from the slopes of $\log(i) vs \log(v)$. Shown in Fig. S3c are the b-values, i.e. 0.92, 0.99, 0.92, 0.99 for the four redox peaks labelled from 1 to 4, respectively. The close-to-1.0 b-values imply that the capacitance dominates the discharge/charge process. Fig. 2b shows that the ratio of capacitive contribution is increased from 83% to 91% with the scan rate increasing from 0.2 to 1 mV s⁻¹. The high capacitive contribution infers fast ion-transport in the bulk of H-VO2 and high-rate capability. To understand the origin of the capacitive contribution, the surface-areanormalized capacitance was calculated using eq. (S3); it was found to be 1.52 F cm⁻² for scan rates between 0.2 to 1 mV s⁻¹, much higher than the conventional double layer capacitance typically in the range of $10\text{--}50~\mu\text{F}~\text{cm}^{\text{--}2}$ [60,61]. Therefore, it is concluded that capacitive behavior seen in H-VO2 is pseudocapacitive in nature, which is the reason for its high rate capability.

To further study the interfacial kinetics of H-VO₂/electrolyte, EIS under open circuit voltage (OCV) was carried out using the same three-electrode system to separate the cathodic contribution from Zn anode. Fig. 2c shows EIS spectra of the H-VO₂/electrolyte interface measured under different temperatures; the equivalent circuit shown in the inset

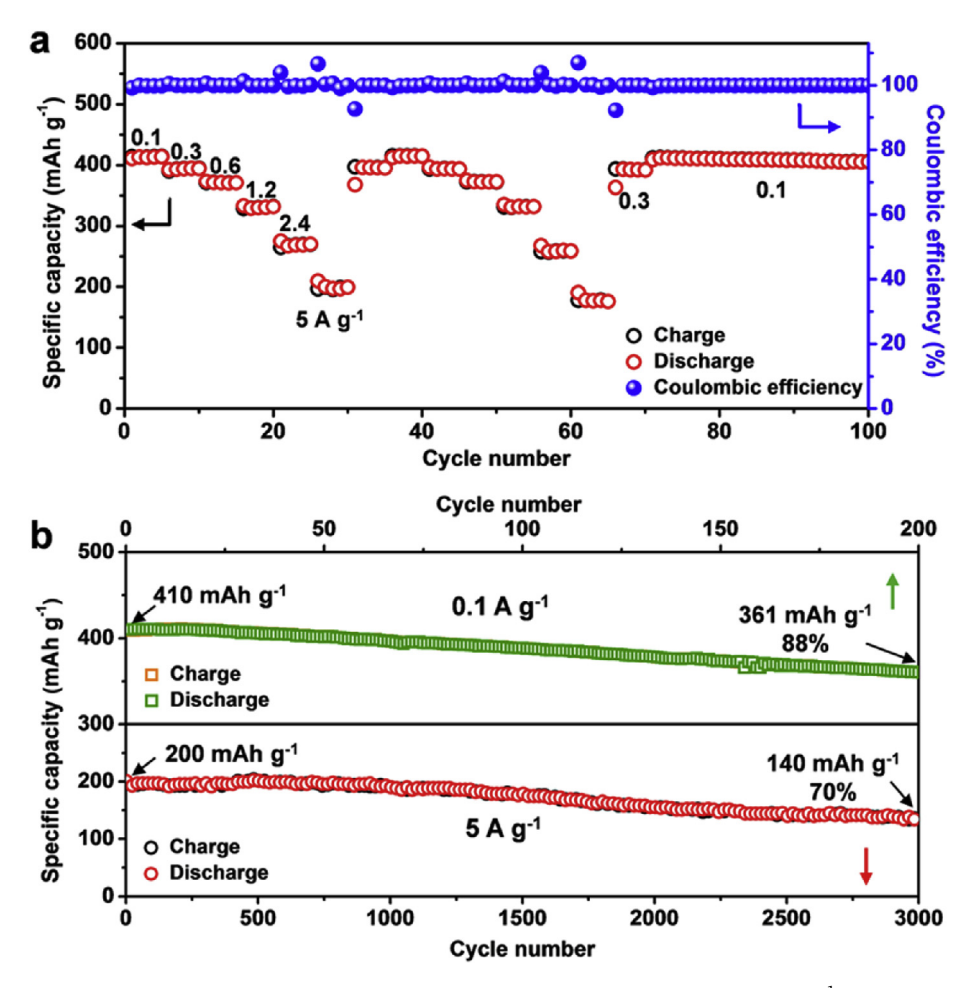


Fig. 3. (a) Rate performance of H-VO₂ at various current densities. (b) Long-term cycling performances of H-VO₂ at 0.1 A g⁻¹ (upper) and 5 A g⁻¹ (lower), respectively.

was used to model the spectra and extract resistances. For example, fitting of EIS spectrum at 298 K (Fig. S4) in a frequency range of 0.1 Hz–100 KHz yields an ohmic resistance R_s of 0.49 Ω (or 0.75 Ω cm²), adsorption-related resistance $R_a=0.84~\Omega$ (or 1.29 Ω cm²) and charge transfer resistance $R_{\rm CT}=19.99~\Omega$ (or 30.76 Ω cm²), showing that $R_{\rm CT}$ is the most significant factor limiting the battery performance. We further plot in Fig. 2d ln ($R_{\rm CT}^{-1}$) versus 1000/T, from the slope of the straight-line the activation energy of charge transfer process is obtained, *i.e.* $E_a=17.8~\rm kJ~mol^{-1}$. This level of $R_{\rm CT}$ and E_a is comparable to that in $H_2V_3O_8$ (20 Ω ; 19.5 kJ mol $^{-1}$) and NaCa $_{0.6}V_6O_{16}\cdot 3H_2O$ (38.4 Ω ; 20.2 kJ mol $^{-1}$) [41,62]. The above CV and EIS analyses on single electrode suggest that H-VO $_2$ is a competitive ZIB cathode with high rate capability benefited from the pronounced pseudocapacitive behavior and fast charge transfer kinetics.

3.3. Electrochemical performance of full H-VO₂/Zn(CF₃SO₃)₂/Zn cell

The electrochemical performances of H-VO $_2$ nanorods cathode in full ZIBs were investigated in coin cells with Zn anode and 3 M Zn(CF $_3$ SO $_3$) $_2$ aqueous electrolyte. Fig. 3a shows the specific discharge/charge capacity at different current densities for the first five cycles; the corresponding galvanostatic discharge/charge curves at these current densities are given in Fig. S5. The specific capacity and current density are calculated based on the mass of H-VO $_2$. With the open circuit voltage (OCV) at \sim 1.25 V, the discharge/charge plateaus of the battery can be easily discerned in Fig. S5a at 0.1 A g $^{-1}$, which is consistent with the redox peaks on the CV curves shown in Fig. 1c. The derived discharge capacities are 414, 395, 372, 332, 270, and 200 mAh g $^{-1}$ at 0.1, 0.3, 0.6, 1.2, 2.4 and 5.0 A g $^{-1}$, respectively, demonstrating its excellent rate capability. Moreover, after changing different current densities for two periods,

99.5% of the capacity is still recoverable when the current density resumes to 0.3 and 0.1 A g $^{-1}$ from 5 A g $^{-1}$. The strong tolerance to the current density infers that H-VO $_2$ has a high structural flexibility and stability against ionic insertions. In addition, Fig. S5b of Ragone plot (energy density νs . powder density) indicates that H-VO $_2$ is the top performer among previously reported ZIB cathodes, such as, V $_2O_5$ [63], Zn $_{0.25}V_2O_5\cdot nH_2O$ [42], H $_2V_3O_8$ [39], K $_2V_6O_{16}\cdot 3H_2O$ [64], NaCa $_{0.6}\cdot V_6O_{16}\cdot 3H_2O$ [41], Zn $_3V_2O_7(OH)_2\cdot 2H_2O$ [44], MnO $_2$ [65], ZnMn $_2O_4$ [36] and Zn $_3$ [Fe(CN) $_6$] $_2$ [26]. To put this into perspective, the H-VO $_2$ delivers an energy density/powder density of 306.3 Wh kg $^{-1}/70.5$ W kg $^{-1}$ and of 142.6 Wh kg $^{-1}/2646$ W kg $^{-1}$ at 0.1 and 5.0 A g $^{-1}$, respectively.

The long-term stability of the battery is further shown in Fig. 3b, where at a low current density of 0.1 A g⁻¹, 88% of the initial capacity is retained after 200 cycles (~1500 h); at a high current density of 5 A g⁻¹, 70% of the initial capacity is retained after 3000 cycles (~215 h). These results again suggest that H-VO₂ possesses excellent structural stability and electrochemical reversibility. Apart from safety, excellent rate capability and cycling stability ensure the battery to be charged/discharged at a fast rate with long cycle life, which is highly desirable for LSRES applications.

3.4. Structural evidences of synergistic dual H^+/Zn^{2+} insertion

To study the ionic storage mechanisms, we first used *in situ* transmission XRD to study phase evolutions of H-VO₂ during a live discharge/charge cycle. Fig. 4a shows the XRD patterns collected from a carbon-paper-supported H-VO₂ electrode over the first cycle at 0.2 A g⁻¹. During the cycle, the peak at 26° remains unchanged, which is attributed to carbon paper (for details see Fig. S6). At OCV state, peaks related to (001)

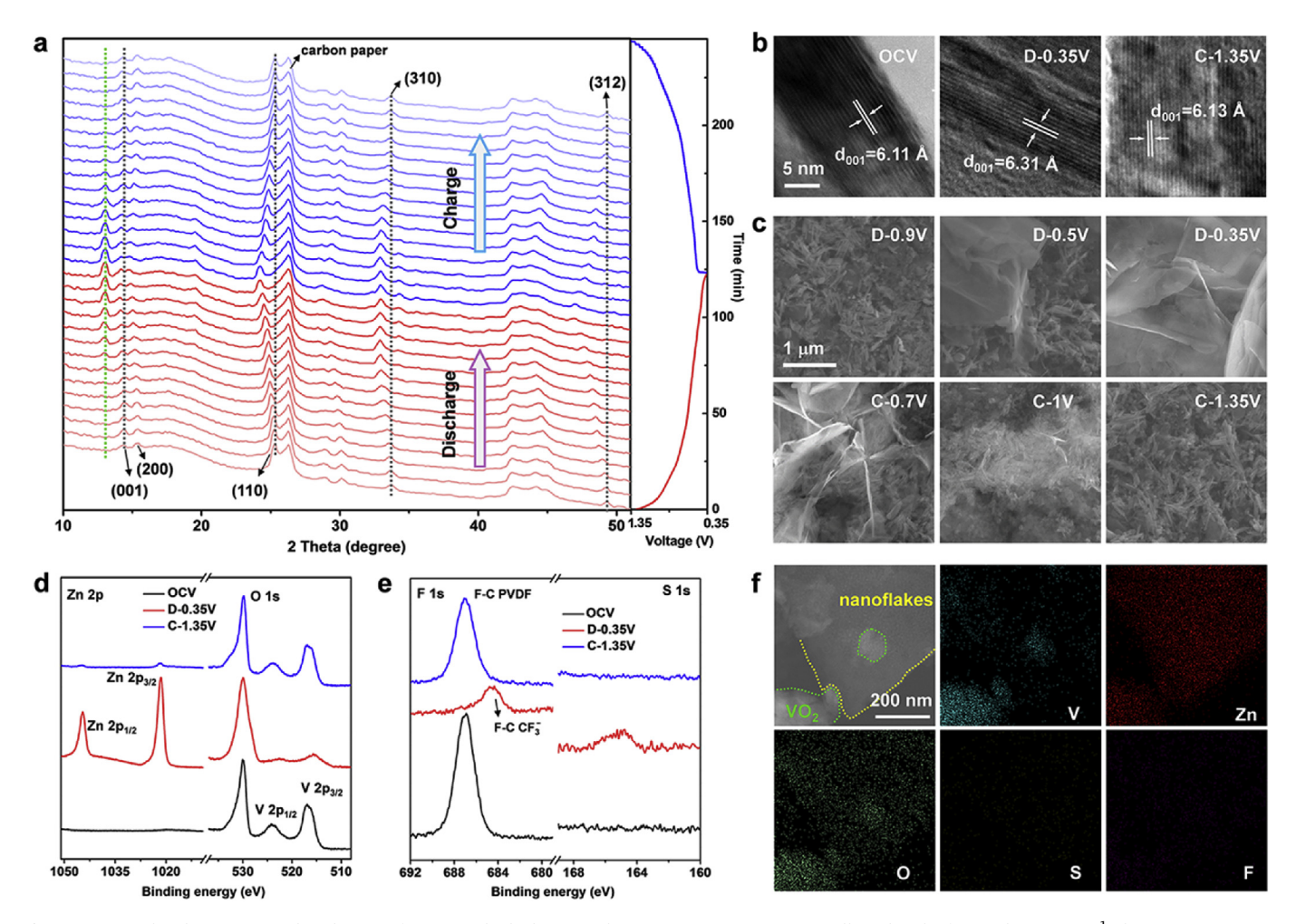


Fig. 4. Structural and compositional evolutions of H-VO₂ cathode during cycling. (a) *In-situ* XRD patterns collected in the first cycle at 0.2 A g⁻¹. (b) HRTEM images at different SOCs. (c) SEM images during cycling. (d) Ex-situ XPS of Zn-2p, O-1s and V-2p at different SOCs. (e) Ex-situ XPS of F-1s and S-1s at different SOCs. (f) STEM images and V, Zn, O, S, and F mappings at the discharged state (D-0.35V). The green and yellow circled areas represent H-VO₂ nanorods and Zn(OH)₂ nanoflakes, respectively. (For interpretation of the references to colour in this figure legend, the reader is referred to the Web version of this article.)

(200) (110) (310) and (312) planes are clearly identified for $H\text{-}VO_2$. These peaks gradually shift toward a lower 2θ during the discharge from OCV to 0.35 V, and then return to the initial position after being charged to 1.35 V, implying that the interplanar spacing of these crystal planes increases during discharge and decreases upon charge. It should be noted that the 2θ of (312) plane changes more than that of (001) and (200) upon discharge according to the Bragg's law [66]:

$$2d\sin\theta = n\lambda\tag{12}$$

where d is the interplanar distance in a crystal; θ is the X-ray incident angle; λ is the X-ray wavelength; n is a positive integer. Differentiating equation of 12 gives:

$$2\Delta d \sin \theta + 2d(\cos \theta)\Delta \theta = 0 \tag{13}$$

$$\Delta\theta = -\frac{\tan\theta}{d} \,\Delta d \tag{14}$$

Therefore, the 2θ at a higher degree such as for (312) plane with a smaller d-value will shift more than that at a lower degree such as (001) and (200) planes upon lattice expansion (Δd) caused by H^+/Zn^{2+} insertion during discharge. To further confirm the changes of interplanar spacing in H-VO₂, HRTEM was performed on H-VO₂ nanorods cycled at different state of charge (SOC). It is evident from Fig. 4b that the (001) d-spacing (d_{001}) of H-VO₂ after discharge is increased to 6.31 Å from 6.11 Å of the pristine H-VO₂ and decreased back to 6.13 Å after charge, in line

with the changes revealed by the *in-situ* XRD. This reversible increase/decrease in the interplanar spacing of crystal planes in response to discharge/charge cycle likely results from the reversible cation insertion/extraction ($\rm Zn^{2+}/H^{+}$), leading to a reversible H-VO₂ tunnel framework expansion/contraction without structural changes.

Interestingly, *in situ* XRD patterns shown in Fig. 4a also reveals a new peak located at ~13° (green dotted line) during discharge, which gradually disappears with charging from 0.35 V to 1.35 V. Fig. 4c of SEM captures the morphological evolution of H-VO₂ cathode *vs* SOC. At first (D-0.9 V), there is no obvious change on the electrode surface, but nanoflakes are observed to gradually emerge with discharging (from D-0.5 V to D-0.35 V) and then gradually vanish during the subsequent charging (from C-0.7 V to C-1.35 V). The close match in trending between the reversible morphological change and the $2\theta = 13^{\circ}$ peak evolution with SOC infers that the new 13° -phase is likely a result of pH hike caused by H⁺ co-insertion during the discharge, while its nanoflake morphology implies a preferential growth of the crystal during pH hike. However, there is no crystallographic evidence to support that the 13° -peak is related to either H_xVO_2 ·0.45H₂O or Zn_vVO_2 ·0.45H₂O.

To investigate the composition of the nanoflakes, ex-situ XPS, SEM-EDS/mapping, STEM-mapping, and HRTEM characterizations were carried out. Firstly, XPS spectra of H-VO $_2$ cathode at different SOCs shown in Fig. 4d indicates a sharp increase in Zn-2p intensity, compared to those at OCV and charged state, suggesting an increased amount of Zn $^{2+}$ in/on the H-VO $_2$ cathode by the discharge, whereas a much smaller V-2p

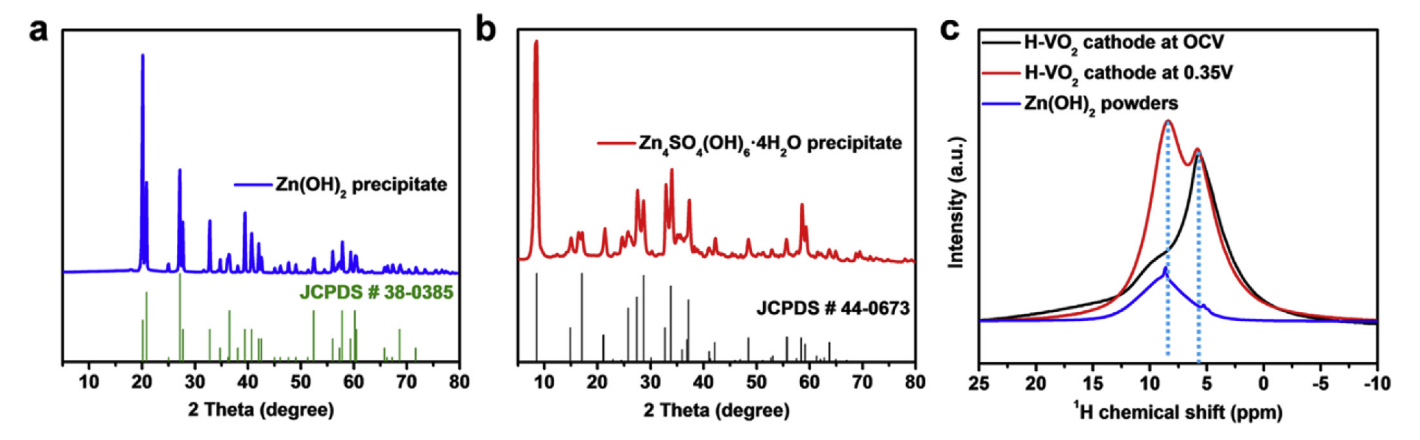


Fig. 5. XRD patterns of the white precipitates formed by adding 1 M NaOH into (a) 3 M Zn(CF₃SO₃)₂ solution and (b) 3 M ZnSO₄ solution, respectively. (c) ¹H NMR spectra of H-VO₂ cathode at different SOCs and pure Zn(OH)₂ powders prepared by adding 1 M NaOH into 3 M Zn(CF₃SO₃)₂ solution. The mass of Zn(OH)₂ powders is about 23% that of H-VO₂ cathode at 0.35V, while the masses of H-VO₂ cathode at OCV and 0.35 V are the same.

intensity at discharged state infers that a nearly V-free layer likely forms and covers the H-VO $_2$ cathode surface, given the fact that H-VO $_2$ contains abundant V. On the other hand, XPS spectra of S-2p and F-1s in Fig. 4e show only very small amounts of S and F on the H-VO $_2$ cathode. These results are also supported by the SEM-mapping and SEM-EDS of H-VO $_2$ cathode at discharge state (D-0.35V) shown in Fig. S7.

The STEM-mapping results collected from samples at discharged state are even more revealing. As shown in Fig. 4f, Figs. S8 and S9, Zn, V and O elements are uniformly distributed in the H-VO₂ nanorods, directly suggesting that $\rm Zn^{2+}$ is inserted into H-VO₂ during discharge; whereas there are mainly Zn and O in the nanoflakes with a slight content of S and F. Since the minor S and F content could derive from the residues of electrolyte or minimal amount of $\rm CF_3SO_3$ inserted into the structure, we here conclude from the combined analysis of XRD (Fig. 4a), HRTEM and

SAED (Fig. S10) that the composition of the nanoflakes is mainly comprised of $Zn(OH)_2$. The finding of $Zn(OH)_2$ is an indication of H^+ insertion into H- VO_2 as the decrease in H^+ concentration in the electrolyte solution can lead to an increase in pH in the electrolyte, ultimately resulting in the formation of $Zn(OH)_2$ [44,59–61].

To verify the above H^+ -insertion mechanism, we also performed several independent experiments. First, we increased pH value of 3 M $Zn(CF_3SO_3)_2$ electrolyte solution by adding 1 M NaOH droplets and immediately we observed $Zn(OH)_2$ precipitates, see Fig. 5a and Fig. S11a. However, the new $2\theta=13^\circ$ XRD peak observed in Fig. 4a after discharge does not match that of the above precipitates shown in Fig. 5a, signaling that they might belong to two different polymorphs of $Zn(OH)_2$ [67]. As aforementioned, this is probably because the $Zn(OH)_2$ nanoflakes are formed preferentially along a specific crystallographic orientation during

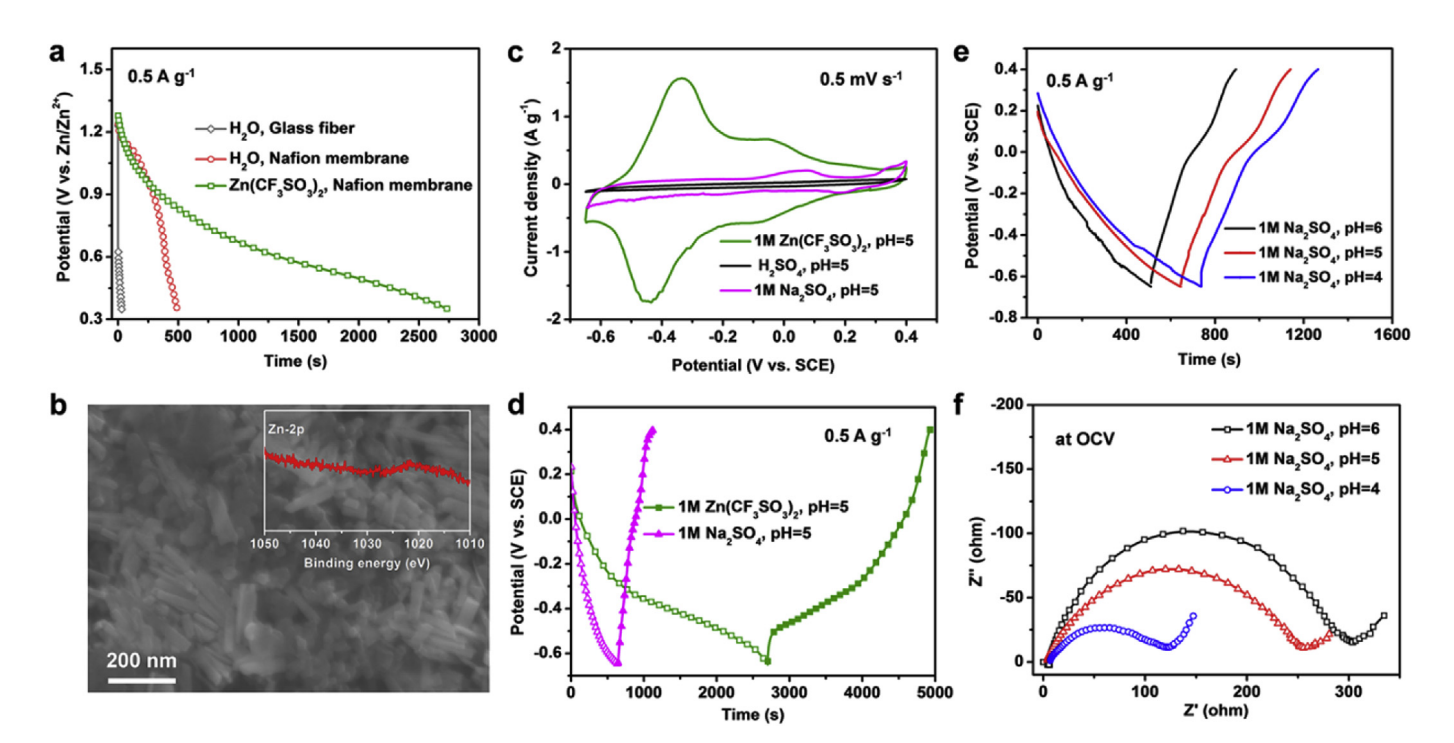


Fig. 6. (a) Discharge curves of H-VO₂ cathode with the different electrolytes (H_2O , $Zn(CF_3SO_3)_2$) and separators (glass fiber, Nafion membrane) using three-electrode system (CE: carbon paper; RE: Zn ring). (b) SEM image of H-VO₂ cathode at fully discharged state (red curve in Figure a) in the system of H_2O electrolyte and Nafion membrane separator. Inset is corresponding Zn-2p XPS spectrum of the H-VO₂ cathode at discharged state. (c) CV curves and (d) discharge and charge curves of H-VO₂ electrode in different electrolytes with the same PH collected from three-electrode system (CE: carbon paper; RE: PCE). (e) Discharge and charge curves and (f) PEIS spectra of PEIS PEIS

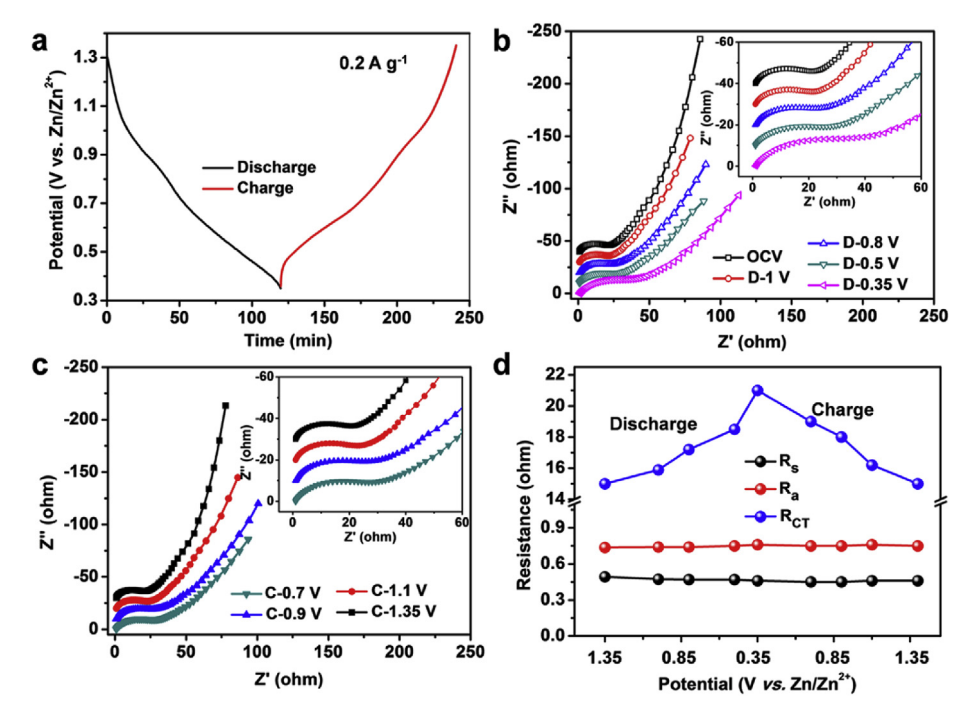


Fig. 7. *In-situ* EIS analysis of H-VO₂ electrode in three-electrode cell (CE: Zn foil; RE: Zn ring). (a) Discharge curve of H-VO₂ cathode in a three-electrode cell at 0.2 A g⁻¹. (b) EIS spectra at different discharged states. (c) EIS spectra at different charged states. (d) Electrolyte resistance R_s, ion-absorption-related resistance R_a, and charge-transfer resistance R_{CT} of H-VO₂ cathodes at different SOCs. Inset in (b) and (c): the magnification of the high/medium-frequency region.

in situ electrochemical process. This result is different from early studies using ZnSO $_4$ electrolyte, in which a Zn $_4$ SO $_4$ (OH) $_6$ ·nH $_2$ O precipitate was reported [48,68–70]. Our experiment indeed confirms the formation of Zn $_4$ SO $_4$ (OH) $_6$ ·nH $_2$ O rather than Zn(OH) $_2$ if 1 M NaOH is added into a 3 M ZnSO $_4$ electrolyte solution, see Fig. 5b and Fig. S11b. Therefore, the type of precipitation product depends on the anion in the Zn-salt, i.e. Zn $_4$ SO $_4$ (OH) $_6$ ·nH $_2$ O for ZnSO $_4$ electrolyte and Zn(OH) $_2$ for Zn(CF $_3$ SO $_3$) $_2$ electrolyte, respectively.

The formation of nanoflake precipitates on the surface of H-VO₂ after discharge is fundamentally derived from the H⁺-insertion. To directly confirm this mechanism, solid state ¹H nuclear magnetic resonance (NMR) was performed on H-VO₂ cathode at pristine state and discharged states; the results are shown in Fig. 5c. The peak at ~5.5 ppm can be assigned to ¹H from the tunnel water in H-VO₂ [63]. Compared to the pristine state, there is an extra strong peak at 8.7 ppm for the discharged state. The spectrum from pure Zn(OH)₂ powders also shows a strong shift at 8.7 ppm, inferring ¹H in Zn(OH)₂ nanoflakes may be responsible for this shift. To further determine if ¹H inserted in H-VO₂ also contributes to this shift, we performed the following simple calculation. The final composition of VO₂ at fully discharged state is HZn_{0.25}VO₂·0.45H₂O, meaning that 1 mol of H⁺-insertion corresponds to 0.5 mol of Zn(OH)₂. Thus, the maximum mass ratio of Zn(OH)2 nanoflakes in the discharged cathode (a mixture of Zn(OH)2, VO2, super P, and PVDF) is only 23%. As shown in Fig. 5c, the peak at 8.7 ppm of pure Zn(OH)2 powders with a similar mass to that of Zn(OH)2 nanoflakes in the discharged cathodes is less intense than the increase caused by changing from pristine state to discharged state. This difference reflects additional contribution to the 8.7 ppm shift from H⁺ inserted in H-VO₂. Therefore, from the structural and compositional analyses vs SOC, it is concluded that both Zn²⁺ and H⁺ are involved in the ionic storage mechanisms of H-VO2 in ZIBs.

3.5. Electrochemical evidences of synergistic dual H^+/Zn^{2+} insertion

Another important supporting evidence for $\mathrm{H^+}$ insertion in $\mathrm{H\text{-}VO_2}$ is provided by electrochemical characterization. To exclude $\mathrm{Zn^{2+}}$ effect on the $\mathrm{H^+}$ insertion, three-electrode cells with $\mathrm{H\text{-}VO_2}$ as working electrode (WE), carbon paper as CE, Zn ring as RE, and Nafion membrane as

separator were assembled with pure H2O and 3 M Zn(CF3SO3)2 as the electrolyte, respectively. The replacement of glass fiber separator by Nafion membrane is due to the much lower ionic conductivity (higher ohmic resistance) of water electrolyte with a glass fiber compared to Nafion membrane (see Fig. S12). Fig. 6a compares the discharge profiles at 0.5 A g⁻¹ for H-VO₂ with Nafion membrane in the two electrolytes (red curve: H₂O; blue curve: 3 M Zn(CF₃SO₃)₂). With the H₂O electrolyte and Nafion membrane, the noticeable discharge capacity (~60 mAh g⁻¹) and reasonable charge transfer resistance (\sim 392 Ω) (see Fig. S12) as well as no Zn element and precipitates observed in/on the discharged H-VO₂ electrode (see Fig. 6b) directly demonstrates that H⁺ can be inserted into H-VO₂ since H⁺ is the only mobile ion in the system. However, the much higher discharge capacity (~380 mAh g⁻¹) shown in Fig. 6a and lower charge transfer resistance (\sim 28 Ω) shown in Fig. S12 with Zn(CF₃SO₃)₂ electrolyte indicate Zn²⁺ insertion into H-VO₂. In addition, we have also performed cycling experiment using an organic solvent electrolyte (1 M Zn(CF₃SO₃)₂ in acetonitrile) to confirm if Zn²⁺ can be intercalated into H-VO₂ without the interference from H⁺. Fig. S13 shows a capacity of 58 mAh g⁻¹ at 0.1 A g⁻¹ can be obtained, even though it is much lower than that with aqueous electrolytes, supporting the possibility of Zn²⁺ insertion in H-VO₂.

To gather the direct evidence for $\mathrm{Zn^{2+}}$ insertion, we ran another set of electrochemical experiments using different electrolytes but at a fixed pH. Fig. 6c and d shows CV and galvanostatic discharge/charge profiles collected from three-electrode system with H-VO₂ as WE, carbon paper as CE, saturated calomel electrode (SCE) as RE. It is evident that the CV area and discharge capacity using $\mathrm{Zn}(\mathrm{CF_3SO_3})_2$ electrolyte are much greater than those using $\mathrm{Na_2SO_4}$ and $\mathrm{H_2SO_4}$, confirming the $\mathrm{Zn^{2+}}$ participation in the reaction during cycle. It is worth noting that the near zero capacity with $\mathrm{H_2SO_4}$ electrolyte at pH = 5 is also due to the very high ohmic resistance (very low ionic conductivity) arising from the very low concentration of $\mathrm{H_2SO_4}$ in the solution (see Fig. S14).

We also performed similar three-electrode electrochemical experiments with an electrolyte without Zn^{2+} to isolate the effect of H^+ . The electrolyte with different pH we selected was Na_2SO_4 aqueous solution with different H_2SO_4 concentrations, while the electrolyte volume was kept at 10 mL. From the discharge/charge curves and EIS at OCV state

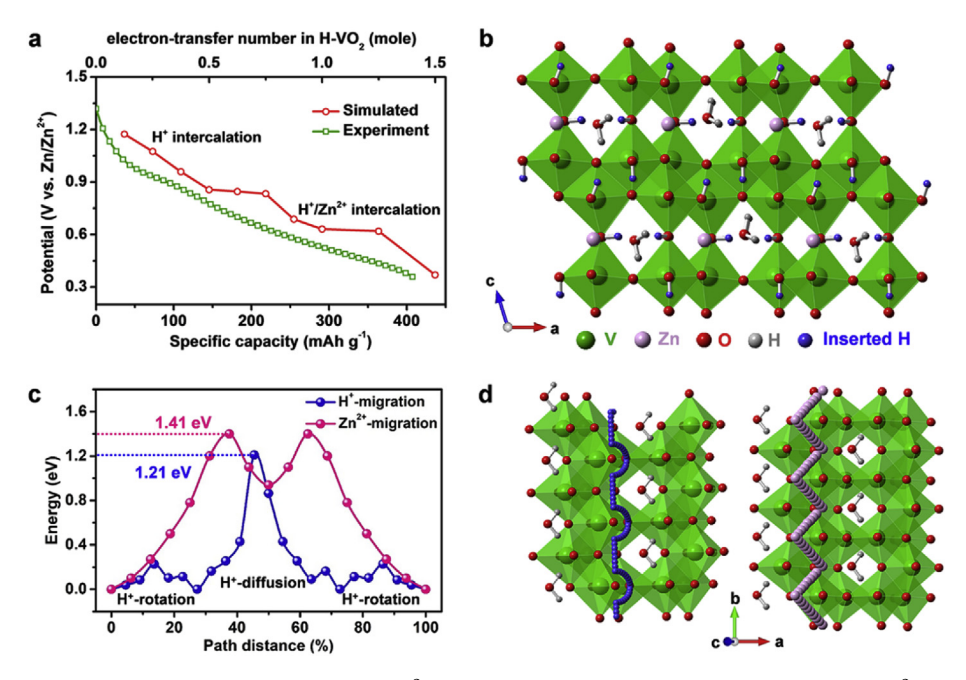


Fig. 8. (a) Simulated and experimental discharge curve with the due Zn^{2+}/H^+ insertion mechanism. (b) The possible sites for Zn^{2+}/H^+ dual insertion. (c) Energy barriers along H^+ - and Zn^{2+} - migration pathways. (d) Migration pathways for H^+ (left) and Zn^{2+} (right) in H-VO₂.

shown in Fig. 6e and f, it is evident that the higher the H^+ concentration the higher the capacity and the lower the charge transfer resistance. Although Na^+ is also insertable into H-VO₂ according to the XPS spectra shown in Fig. S15, the concentration of Na^+ in the three electrolytes are the same and the only difference is the concentration of H^+ . Therefore, the differences in capacity and charge-transfer resistance are a direct result of H^+ concentration (pH), which confirms that H^+ is insertable into H-VO₂ cathode.

To study how the formation of nanoflakes affect the interfacial Zn²⁺/ H⁺ insertion kinetics, we ran a series of in-situ EIS measurements using three-electrode cell. The three-electrode cell with H-VO2 WE, Zn foil CE, Zn ring RE were cycled to different potentials at 0.2 A g⁻¹ (see Fig. 7a) and held at the potential for 1 h to reach equilibrium before the EIS measurements. The original EIS spectra of H-VO2 electrode at different SOCs are given in Fig. 7b and c and fitted by an equivalent circuit shown in the inset of Fig. 2c and Fig. S16. The extracted values shown in Fig. 7d indicate that the electrolyte resistance (R_s) and Zn²⁺/H⁺-absorptionrelated resistance are small and remain as constants (\sim 0.5 Ω and \sim 0.8 Ω), compared to R_{CT}, suggesting the nanoflakes have no significant effect on the ionic conductivity of the electrolyte and Zn²⁺/H⁺-absorption process. In contrast, R_{CT} is seen to gradually increase from 15 Ω in the initial OCV state to 21.0 Ω at the fully discharged state (0.35 V), and then gradually decreases in the subsequent charge process to the initial value (15 Ω) at the fully charge state. Interestingly, this trending follows well with the evolution of Zn(OH)2 nanoflakes, implying that the formation of Zn(OH)2 nanoflakes does have an impact on RCT, but it is reversible and unharmful to cycle life. Similar trend was also observed in Li/Na ion batteries, but the change in R_{CT} for $Li_xNi_{1-y}Co_yO_2$ and CoZnS cathode in Li/Na ion batteries during cycle is \sim 500 Ω and \sim 100 Ω , respectively, much higher than that for H-VO₂ (6 Ω) in ZIB [71,72].

3.6. Understanding the synergistic dual H^+/Zn^{2+} insertion mechanisms by DFT

To support the dual $\rm H^+/Zn^{2+}$ insertion mechanisms, we also carried out a detailed first-principle calculation aiming to elucidate the energetics and pathways of $\rm H^+/Zn^{2+}$ insertion into the $\rm H\text{-}VO_2$ structure. Fig. 8a shows a simulated discharge curve considering dual $\rm H^+/Zn^{2+}$ insertion and its comparison with the experimental data, verifying the

strong possibility of dual H^+/Zn^{2+} insertion. Note that Figs. S17a and 17b show that consideration of Zn^{2+} -only insertion into H-VO₂ cannot produce a capacity matching to the experimental data, i.e. 140 mAh g⁻¹ vs. 414 mAh g⁻¹. On the other hand, Figs. S17c and 17d indicate that consideration of H⁺-only insertion into H-VO₂ can produce a capacity matching to the experimental data at high voltage regime (V > 0.9V), but not at low voltage regime (V < 0.9V).

The possible sites for H^+/Zn^{2+} -insertion in $H\text{-}VO_2$ are shown in Fig. 8b, where there are eight H^+ -sites and two Zn^{2+} -sites in the computation cell (eight $VO_2\cdot 0.5H_2O$ units). The composition of final product for the dual Zn^{2+}/H^+ insertion into $H\text{-}VO_2$ is deemed as $HZn_{0.25}VO_2\cdot 0.5H_2O$ and the corresponding theoretical capacity is 436.5 mAh g^{-1} . The calculations also show that the diffusion barriers of Zn^{2+} and H^+ are 1.41 and 1.21 eV, respectively. The difference in diffusion barriers between Zn^{2+} and H^+ infers that the fast-moving H^+ insertion may dominate at high voltages, whereas slow-moving Zn^{2+} insertion may control at low voltages. This conclusion seems to be supported by Fig. S18, where the GITT-derived diffusion coefficient is higher at lower capacity. For pathways, Fig. 8d suggests that Zn^{2+} prefers to migrate along a zigzag path in H-VO2, while H^+ -diffusion in H-VO2 follows a pathway involving first rotation around O atom and then migration along the b direction between O atoms.

Based on the above analysis, the electrochemical reactions of $H-VO_2/Zn(CF_3SO_3)_2/Zn$ cell (based on the theoretical capacity) can be summarized as follows:

Anode:

$$3Zn \leftrightarrow 3Zn^{2+} + 6e^{-} \tag{15}$$

Cathode:

$$4H_2O \leftrightarrow 4H^+ + 4OH^-$$
 (16)

$$4VO_2 \cdot 0.45 H_2O + 4H^+ + Zn^{2+} + 6e^- \leftrightarrow 4(HZn_{0.25})VO_2 \cdot 0.45 H_2O$$
 (17)

$$2Zn^{2+} + 4OH^{-} \leftrightarrow 2Zn(OH)_{2} \downarrow \tag{18}$$

The overall reaction is:

 $4VO_2 \cdot 0.45 \ H_2O + 4H_2O + 3Zn \leftrightarrow 4(HZn_{0.25})VO_2 \cdot 0.45 \ H_2O + 2Zn(OH)_2 \downarrow$ (19)

It is important to mention that the Zn^{2+}/H^+ storage mechanism in H-VO₂ is different from the dissolution/deposition mechanism in Zn/MnO₂ batteries with a Zn^{2+}/Mn^{2+} electrolyte where Mn^{2+} is oxidized to MnO_2 during charge and the latter is re-dissolved during discharge [30–36].

4. Conclusion

In summary, H-VO2 nanorods have been systematically studied as a potential cathode material for rechargeable aqueous ZIBs and a model material for understanding the ionic storage mechanisms. The electrochemical testing shows that H-VO2 cathode exhibits a strong pseudocapacitive behavior and its capacity can reach 410 and 200 mAh g⁻¹, while maintaining 88% and 70% of its capacity after 200 cycles (~1500 h) and 3000 cycles (~215 h) at 0.1 A g⁻¹ and 5 A g⁻¹, respectively. The mechanistic study complemented by three-electrode electrochemical CV and EIS measurements, in-situ transmissive XRD, XPS, HRTEM, STEM and ¹H NMR reveals that the ionic storage capacity achieved is attributed to a synergistic H⁺ and Zn²⁺ co-insertion mechanism. In specific, DFT calculations reproduce a similar discharge curve to the experimental one with the consideration of dual Zn²⁺/H⁺ insertion and predict that H⁺insertion predominates at high voltage regime (initial discharge stage) whereas Zn²⁺/H⁺-insertion controls at low voltage regime (late discharge stage). The study also confirms by in-situ XRD and ex-situ SEM that H⁺ insertion is accompanied by the formation of nanoflakes precipitates having a composition close to Zn(OH)₂ on the surface of H-VO₂ due to the increased pH in the electrolyte. However, Zn(OH)₂ precipitates are dissolvable upon charging and do not affect the charge-transfer process during cycling, enabling the reversibility of H-VO2 as a ZIB cathode. Therefore, H⁺-insertion is synergistic to Zn²⁺-insertion and can be viewed as an indirect Zn²⁺-storage in the form of Zn(OH)₂. Overall, the demonstrated high-capacity and ultra-stability promises H-VO2 to be a strong candidate cathode for ZIBs. The fundamental insights gained from this study deepen the current understanding of aqueous Zn-ion battery chemistry in neutral aqueous electrolytes and lay foundation for future discovery of new better ZIB cathodes.

Declaration of competing interest

The authors declare no conflict of interest.

CRediT authorship contribution statement

Kaiyue Zhu: Data curation, Formal analysis, Writing - original draft. Tao Wu: Data curation, Formal analysis, Writing - original draft. Shichen Sun: Formal analysis. Wessel van den Bergh: Data curation. Morgan Stefik: Formal analysis. Kevin Huang: Data curation, Formal analysis, Writing - original draft.

Acknowledgements

K.Z., T.W., S.S. and K.H. thank South Carolina SmartState Center program and National Science Foundation under award number CBET-1801284 for financial support. W.V.D.B. and M.S. acknowledge support by the National Science Foundation (DMR-1752615). This work made use of the South Carolina SAXS Collaborative.

Appendix A. Supplementary data

Supplementary data to this article can be found online at https://do i.org/10.1016/j.ensm.2020.03.030.

References

- [1] S. Chu, A. Majumdar, Nature 488 (2012) 294-303.
- [2] M. Song, H. Tan, D. Chao, H.J. Fan, Adv. Funct. Mater. 28 (2018) 1802564.
- [3] J. Ming, J. Guo, C. Xia, W. Wang, H.N. Alshareef, Mater. Sci. Eng. R 135 (2019) 58–84
- [4] J. Huang, Z. Guo, Y. Ma, D. Bin, Y. Wang, Y. Xia, Small Methods 3 (2019) 1800272.
- [5] G. Fang, J. Zhou, A. Pan, S. Liang, ACS Energy Lett. 3 (2018) 2480–2501.
- [6] Z. Xing, S. Wang, A. Yu, Z. Chen, Nano Energy 50 (2018) 229–244.
- [7] W. Lu, C. Xie, H. Zhang, X. Li, ChemSusChem 11 (2018) 3996-4006.
- [8] T.H. Wu, Y. Zhang, Z.D. Althouse, N. Liu, Mater. Today Nano 6 (2019) 100032.
- [9] Q. Yang, G. Liang, Y. Guo, Z. Liu, B. Yan, D. Wang, Z. Huang, X. Li, J. Fan, C. Zhi, Adv. Mater. 9 (2019) 1903778.
- [10] P. He, Q. Chen, M. Yan, X. Xu, L. Zhou, L. Mai, C.-W. Nan, EnergyChem 1 (2019) 100022.
- [11] Y. Wu, Y. Zhang, Y. Ma, J.D. Howe, H. Yang, P. Chen, S. Aluri, N. Liu, Adv. Energy Mater. 8 (2018) 1802470.
- [12] Y. Li, J. Fu, C. Zhong, T. Wu, Z. Chen, W. Hu, K. Amine, J. Lu, Adv. Energy Mater. 9 (2019) 1802605.
- [13] A. Konarov, N. Voronina, J.H. Jo, Z. Bakenov, Y.-K. Sun, S.-T. Myung, ACS Energy Lett. 3 (2018) 2620–2640.
- [14] B. Tang, L. Shan, S. Liang, J. Zhou, Energy Environ. Sci. 12 (2019) 3288-3304.
- [15] K. Zhu, T. Wu, K. Huang, ACS Nano 13 (2019) 14447-14458.
- [16] X. Zeng, J. Hao, Z. Wang, J. Mao, Z. Guo, Energy Storage Mater. 20 (2019) 410–437
- [17] P. He, M. Yan, G. Zhang, R. Sun, L. Chen, Q. An, L. Mai, Adv. Energy Mater. 7 (2017) 1601920.
- [18] D. Chao, C.R. Zhu, M. Song, P. Liang, X. Zhang, N.H. Tiep, H. Zhao, J. Wang, R. Wang, H. Zhang, H.J. Fan, Adv. Mater. 30 (2018) 1803181.
- [19] F. Wang, E. Hu, W. Sun, T. Gao, X. Ji, X. Fan, F. Han, X.-Q. Yang, K. Xu, C. Wang, Energy Environ. Sci. 11 (2018) 3168–3175.
- [20] Y. Yang, Y. Tang, G. Fang, L. Shan, J. Guo, W. Zhang, C. Wang, L. Wang, J. Zhou, S. Liang, Energy Environ. Sci. 11 (2018) 3157–3162.
- [21] F. Wan, L. Zhang, X. Dai, X. Wang, Z. Niu, J. Chen, Nat. Commun. 9 (2018) 1656.
- [22] P. He, Y. Quan, X. Xu, M. Yan, W. Yang, Q. An, L. He, L. Mai, Small 13 (2017) 1702551.
- [23] L. Wang, K.-W. Huang, J. Chen, J. Zheng, Sci. Adv. 5 (2019) eaax4279.
- [24] P. Hu, T. Zhu, X. Wang, X. Zhou, X. Wei, X. Yao, W. Luo, C. Shi, K.A. Owusu, L. Zhou, L. Mai, Nano Energy 58 (2019) 492–498.
- [25] G. Li, Z. Yang, Y. Jiang, C. Jin, W. Huang, X. Ding, Y. Huang, Nano Energy 25 (2016) 211–217.
- [26] L. Zhang, L. Chen, X. Zhou, Z. Liu, Adv. Energy Mater. 5 (2015) 1400930.
- [27] R. Trocoli, F. La Mantia, ChemSusChem 8 (2015) 481-485.
- [28] C. Xu, B. Li, H. Du, F. Kang, Angew. Chem. Int. Ed. 51 (2012) 933–935.
- [29] M.H. Alfaruqi, V. Mathew, J. Gim, S. Kim, J. Song, J.P. Baboo, S.H. Choi, J. Kim, Chem. Mater. 27 (2015) 3609–3620.
- [30] M.H. Alfaruqi, J. Gim, S. Kim, J. Song, D.T. Pham, J. Jo, Z. Xiu, V. Mathew, J. Kim, Electrochem. Commun. 60 (2015) 121–125.
- [31] X. Guo, J. Zhou, C. Bai, X. Li, G. Fang, S. Liang, Mater. Today Energy 16 (2020) 100396.
- [32] C. Xie, T. Li, C. Deng, Y. Song, H. Zhang, X. Li, Energy Environ. Sci. 23 (2020) 134–143.
- [33] D. Chao, W. Zhou, C. Ye, Q. Zhang, Y. Chen, L. Gu, K. Davey, S.Z. Qiao, Angew. Chem. Int. Ed. 58 (2019) 7823–7828.
- [34] W. Sun, F. Wang, S. Hou, C. Yang, X. Fan, Z. Ma, T. Gao, F. Han, R. Hu, M. Zhu, C. Wang, J. Am. Chem. Soc. 139 (2017) 9775–9778.
- [35] H. Pan, Y. Shao, P. Yan, Y. Cheng, K.S. Han, Z. Nie, C. Wang, J. Yang, X. Li, P. Bhattacharya, K.T. Mueller, J. Liu, Nat. Energy 1 (2016) 16039.
- [36] N. Zhang, F. Cheng, Y. Liu, Q. Zhao, K. Lei, C. Chen, X. Liu, J. Chen, J. Am. Chem. Soc. 138 (2016) 12894–12901.
- [37] Y. Zeng, Z. Lai, Y. Han, H. Zhang, S. Xie, X. Lu, Adv. Mater. 30 (2018) 1802396.
- [38] J. Ding, Z. Du, L. Gu, B. Li, L. Wang, S. Wang, Y. Gong, S. Yang, Adv. Mater. 30 (2018) 1800762.
- [39] Q. Pang, C. Sun, Y. Yu, K. Zhao, Z. Zhang, P.M. Voyles, G. Chen, Y. Wei, X. Wang, Adv. Energy Mater. 8 (2018) 1800144.
- [40] P. Hu, T. Zhu, X. Wang, X. Wei, M. Yan, J. Li, W. Luo, W. Yang, W. Zhang, L. Zhou, Z. Zhou, L. Mai, Nano Lett. 18 (2018) 1758–1763.
- [41] K. Zhu, T. Wu, K. Huang, Adv. Energy Mater. 9 (2019) 1901968.
- [42] D. Kundu, B.D. Adams, V. Duffort, S.H. Vajargah, L.F. Nazar, Nat. Energy 1 (2016)
- [43] C. Xia, J. Guo, P. Li, X. Zhang, H.N. Alshareef, Angew. Chem. Int. Ed. 57 (2018) 3943–3948.
- [44] C. Xia, J. Guo, Y. Lei, H. Liang, C. Zhao, H.N. Alshareef, Adv. Mater. 30 (2018) 1705580.
- [45] F. Wang, W. Sun, Z. Shadike, E. Hu, X. Ji, T. Gao, X.Q. Yang, K. Xu, C. Wang, Angew. Chem. Int. Ed. 57 (2018) 11978–11981.
- [46] L. Chen, Y. Ruan, G. Zhang, Q. Wei, Y. Jiang, T. Xiong, P. He, W. Yang, M. Yan, Q. An, L. Mai, Chem. Mater. 31 (2019) 699–706.
- [47] J.-S. Park, J.H. Jo, Y. Aniskevich, A. Bakavets, G. Ragoisha, E. Streltsov, J. Kim, S.-T. Myung, Chem. Mater. 30 (2018) 6777–6787.
- [48] Z. Li, S. Ganapathy, Y. Xu, Z. Zhou, M. Sarilar, M. Wagemaker, Adv. Energy Mater. 9 (2019) 1900237.
- [49] A. Pan, H.B. Wu, L. Yu, T. Zhu, X.W. Lou, ACS Appl. Mater. Interfaces 4 (2012) 3874–3879.
- [50] X. Guo, G. Fang, W. Zhang, J. Zhou, L. Shan, L. Wang, C. Wang, T. Lin, Y. Tang, S. Liang, Adv. Energy Mater. 8 (2018) 1801819.

- [51] P. Hohenberg, W. Kohn, Phys. Rev. 136 (1964) B864-B871.
- [52] W. Kohn, L.J. Sham, Phys. Rev. 140 (1965) A1133-A1138.
- [53] G. Kresse, J. Furthmüller, Phys. Rev. B 54 (1996) 11169-11186.
- [54] J.P. Perdew, K. Burke, M. Ernzerhof, Phys. Rev. Lett. 77 (1996) 3865-3868.
- [55] P.E. Blöchl, Phys. Rev. B 50 (1994) 17953-17979.
- [56] V.I. Anisimov, F. Aryasetiawan, A.I. Lichtenstein, J. Phys. Condens. Matter 9 (1997) 767–808.
- [57] S. Grimme, S. Ehrlich, L. Goerigk, J. Comput. Chem. 32 (2011) 1456–1465.
- [58] S. Adams, R.P. Rao, Phys. Status Solidi A 208 (2011) 1746-1753.
- [59] S. Smidstrup, A. Pedersen, K. Stokbro, H. Jonsson, J. Chem. Phys. 113 (2014) 9901–9904.
- [60] T. Brousse, D. Be'Langer, J.W. Long, J. Electrochem. Soc. 162 (2015) A5185–A5189.
- [61] J. Wang, J. Polleux, J. Lim, B. Dun, J. Phys. Chem. C 111 (2007) 14925-14931.
- [62] D. Kundu, S. Hosseini Vajargah, L. Wan, B. Adams, D. Prendergast, L.F. Nazar, Energy Environ. Sci. 11 (2018) 881–892.

- [63] M. Yan, P. He, Y. Chen, S. Wang, Q. Wei, K. Zhao, X. Xu, Q. An, Y. Shuang, Y. Shao, K.T. Mueller, L. Mai, J. Liu, J. Yang, Adv. Mater. 30 (2018) 1703725.
- [64] B. Sambandam, V. Soundharrajan, S. Kim, M.H. Alfaruqi, J. Jo, S. Kim, V. Mathew, Y.-k. Sun, J. Kim, J. Mater. Chem. A 6 (2018) 15530–15539.
- [65] N. Zhang, F. Cheng, J. Liu, L. Wang, X. Long, X. Liu, F. Li, J. Chen, Nat. Commun. 8 (2017) 405.
- [66] W.H. Bragg, W.L. Bragg, Proc. Roy. Soc. Lond. A 88 (605) 428-438.
- [67] A.M. Clark, E.E. Fejer, G. Cressey, P.C. Tandy, Mineral. Mag. 52 (1988) 699-702.
- [68] J. Huang, Z. Wang, M. Hou, X. Dong, Y. Liu, Y. Wang, Y. Xia, Nat. Commun. 9 (2018) 2906.
- [69] P. Oberholzer, E. Tervoort, A. Bouzid, A. Pasquarello, D. Kundu, ACS Appl. Mater. Interfaces 11 (2019) 674–682.
- [70] Y. Li, S. Wang, J.R. Salvador, J. Wu, B. Liu, W. Yang, J. Yang, W. Zhang, J. Liu, J. Yang, Chem. Mater. 31 (2019) 2036–2047.
- [71] F. Nobili, F. Croce, B. Scrosati, R. Marassi, Chem. Mater. 13 (2001) 1642–1646.
- [72] G. Fang, Z. Wu, J. Zhou, C. Zhu, X. Cao, T. Lin, Y. Chen, C. Wang, A. Pan, S. Liang, Adv. Energy Mater. 8 (2018) 1703155.